J. Fluid Mech. (1989), *vol.* 209, *pp.* 309–334
Printed in Great Britain

Spatio-temporal regimes in Rayleigh–Bénard convection in a small rectangular cell

By M. A. RUBIO†, P. BIGAZZI, L. ALBAVETTI AND S. CILIBERTO

Istituto Nazionale di Ottica, Largo Enrico Fermi 6, 50125 Arcetri-Firenze, Italy

(Received 28 July 1988 and in revised form 3 April 1989)

By means of an original optical technique we have studied the spatio-temporal behaviour in a Rayleigh–Bénard convection experiment of small rectangular geometry. The experimental technique allows complete reconstruction of the temperature field integrated along the roll axis. Two main spatiotemporal regimes have been found, corresponding to localized oscillations and travelling waves respectively. Several parameters are proposed for the quantitative characterization of this complex behaviour.

1. Introduction

During recent years Rayleigh–Bénard convection has been widely used to study a large number of nonlinear problems that range from pattern selection (Krishnamurti 1970*a*; Stork & Müller 1972; Gollub & McCarriar 1982; Pocheau, Corquette & Le Gal 1985; Heutmaker, Fraenkel & Gollub 1985; Ahlers, Cannel & Steinberg 1985) to transition from regular to chaotic behaviour (Krishnamurti 1970*b*; Gollub & Benson 1980; Libchaber, Laroche & Fauve 1982; Dubois, Rubio & Berge 1983).

To illustrate the first stages of Rayleigh–Bénard instability let us consider a horizontal fluid layer confined in a rectangular box. When heated from below a competition between buoyancy force, viscous damping and heat diffusion is established. Upon progressively increasing the control parameter, i.e. the temperature difference ΔT between the two horizontal plates, convection begins at a certain critical value. A periodic structure appears in the form of a set of parallel rolls with wavenumber q. For a fluid layer confined between conducting plates, with infinite horizontal extent, $q = 3.1/d$, where d is the depth of the fluid layer (for a detailed study see, for example, Chandrasekhar 1961; Busse & Whitehead 1971; Normand, Pomeau & Velarde 1977; Busse 1978).

The most relevant parameters in Rayleigh–Bénard instability are the Rayleigh number $R = \alpha g \Delta T d^3/\nu\kappa$, that accounts for the imposed temperature gradient, the Prandtl number $Pr = \nu/\kappa$ that characterizes the fluid, accounting for the relation between the vorticity and heat diffusion coefficients, and finally the aspect ratio $\Gamma = L/d$ where L and d are, respectively, the horizontal and vertical lengthscales of the container. In the definitions of these parameters α, g, ν and κ represent, respectively, the volumetric expansion coefficient, the acceleration due to gravity, the kinematic viscosity and the thermal diffusivity.

Upon further increasing R above the critical value R_c ($R_c = 1708$ for the conditions

† Permanent address: Departamento de Fisica Fundamental, Facultad de Ciencias. U.N.E.D., Aptdo. Correos 60141. Madrid, 28080, Spain.

above), the response of the system strongly depends on Γ. If Γ is small the fluid confinement by the lateral walls is very high and the roll structure is not allowed to undergo great changes. On the other hand if Γ is large the spatial structure is quite free to change and usually the original regular roll pattern soon becomes distorted by local defects, grain boundaries and dislocations.

In large-aspect-ratio containers most of the experimental observations show that the spatial pattern evolution near threshold is in good agreement with theories (Pocheau *et al.* 1985; Heutmaker *et al.* 1985; Ahlers *et al.* 1985). However this type of cell does not seem to be suitable for studies of transition to temporal chaos.

For small-aspect-ratio cells the situation is the opposite: it has been fully demonstrated by experiments that very often the time-dependent states can be described by low-dimensional attractors, either periodic or strange. However, most of these observations were done by measuring a local variable in a fixed position.

In the frame just described, the problem of the coupling between temporal behaviour and spatial structure still remains to be solved. In order to understand the transition from regular to turbulent flow, the study of the relationship between spatial and temporal degrees of freedom in a fluid system is essential. This study should clarify the role of some low-dimensional chaotic states as precursors of turbulence.

The relationship between spatial order and temporal chaos has been recently investigated with different approaches. Numerical studies are available for several systems that cover the Boussinesq equations for Rayleigh–Bénard convection (Curry *et al.* 1984; Bolton, Busse & Clever 1986), some simple models of partial differential equations (Bishop *et al.* 1983; Hyman & Nicolaenko 1986; Cháté & Manneville 1987), systems of coupled maps (Kaneko 1985; Oppo & Kapral 1986), and chemical reactions (Oono & Kohmoto 1985).

Experimentally, some of these aspects have been studied in different systems like the baroclinic waves in a rotating differentially heated annulus (Buzyna, Pfeffer & Kung 1984) and convection in a Hele-Shaw slot (Koster & Müller 1984). In an experiment on surface wave instabilities it has been shown that spatial mode competition is one of the mechanisms leading to chaotic behaviour (Ciliberto & Gollub 1984, 1985; Simonelli & Gollub 1988, 1989).

Furthermore, in Rayleigh–Bénard convection some relevant spatial features of the low-dimensional transitions to chaos have been reported, mainly concerning the localization of oscillators (Krishnamurti 1970*b*; Dubois & Berge 1981; Dubois *et al.* 1983; Walden *et al.* 1984). Very recently travelling waves have been found both in small-Γ cells far above onset (Ciliberto & Rubio 1987*a*) and in convection in binary mixtures very near threshold (Kolodner *et al.* 1986*a*; Moses & Steinberg 1986).

In spite of these advances there are still many open questions on the number of oscillating modes, the frequency at which they oscillate or the way in which energy is distributed among them. Furthermore, as far as the characterization of low-dimensional chaos is concerned, there are still some open problems related to the spatial structure of the chaotic behaviour (Vastano & Swinney 1988).

Let us briefly review the main tools available for the characterization process. The temporal features are usually analysed by means of bifurcation diagrams, return maps and power spectra.

Another way to look at chaotic regimes is to study their geometrical properties in phase space. Strange attractors are characterized by fractal dimension and metric entropy and several methods have been proposed to compute them from experimental time series (Farmer, Ott & Yorke 1983; Grassberger & Procaccia 1983;

Badii & Politi 1985). Fractal dimension roughly estimates the number of relevant variables involved in the process, while metric entropy measures the average rate of information loss per unit time, and both may be used to discriminate between low-dimensional chaos and purely stochastic phenomena (Malraison *et al.* 1983; Giglio, Musazzi & Perini 1984; Ciliberto & Gollub 1985).

In most of the experiments the computation of fractal dimension and metric entropy is done on the data of a single scalar variable invoking the embedding theorem (Takens 1981; Farmer *et al.* 1983). This scalar signal is usually obtained from either the local measurement of a variable (e.g. horizontal temperature gradient, vertical component of the velocity) or from the measurement of a spatially averaged variable (e.g. total heat flux, total electric current in electroconvection).

Another way of constructing the phase space for the computations is to measure a local variable simultaneously at many points and to build up a vectorial variable with these time series (Guckenheimer & Buzyna 1983). Very recent results (Ciliberto 1987) have thrown some light on several questions that could be raised, such as is there any spatial dependence of FD for local measurements or are the results obtained for spatially averaged variables equivalent to those obtained for local measurements?

Turning to the study of spatiotemporal regimes, the usual tools are Fourier transforms both in space and time (Bishop *et al.* 1983) and spatiotemporal correlation functions (Ciliberto & Rubio 1987*a*). Unfortunately both techniques yield qualitative results that are good for identifying different behaviours but do not allow quantitative comparison between different regimes.

Proceeding from this framework, the aim of this paper is to extend these previous studies on the relationship between spatial structure and temporal chaos. For this purpose experiments were performed in a Rayleigh–Bénard convective system with rectangular geometry and $\Gamma = 4$. In more detail our objectives are twofold. First we examine the space–time evolution of the temperature field, focusing our attention on identifying the structures as localized or distributed in space and on examining the transition between them. Second, we propose to use in this context some parameters that allow for quantitative analysis of spatiotemporal regimes. To achieve these goals the temperature field is measured by means of an optical scanning beam deflection technique (Ciliberto, Francini & Simonelli 1985).

This paper is organized as follows. In §2 we describe the apparatus, the beam deflection technique and the experimental procedure. In §3 we introduce some parameters that can help in the quantitative study of spatio-temporal regimes. Then in §4 the results concerning spatio-temporal behaviour are given and the analysis and characterization of the structures (in terms of time-resolved spatial Fourier transforms) are discussed. Finally, conclusions are presented in §5.

2. The experimental set-up

2.1. *The convection cell*

The experiments were conducted in a rectangular cell of dimensions $l_x = 4$ cm, $l_y = 1$ cm and $d = 1$ cm, giving then $\Gamma_x = 4$, $\Gamma_y = 1$. The x and y horizontal axes of the coordinate reference frame are respectively perpendicular and parallel to the roll axis, while the z-axis is vertical.

A schematic view of the cell and the thermal regulation system is displayed in figure 1. The upper and lower boundaries are copper plates 1 cm thick (CU), where two very narrow holes (0.07 cm diameter) have been drilled in opposite locations to

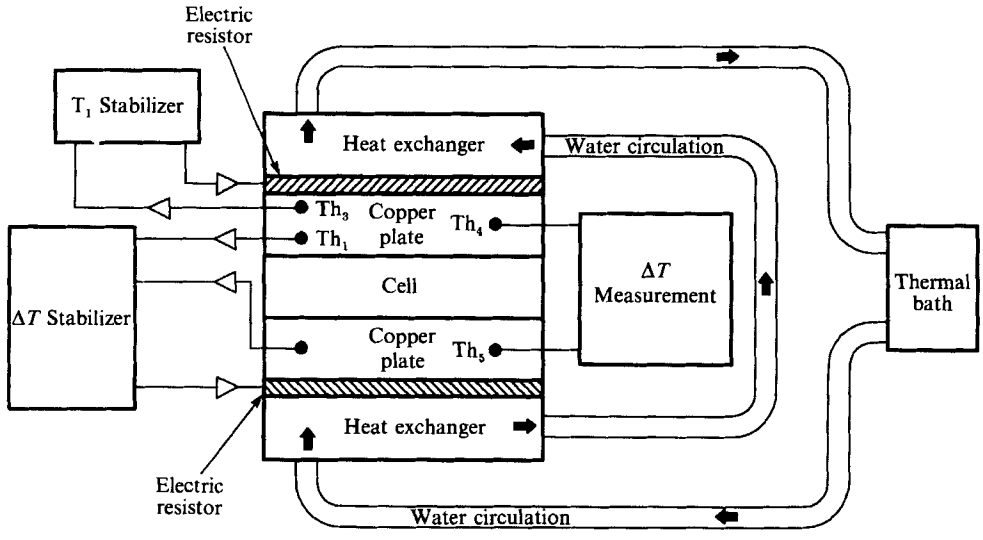

FIGURE. 1. Schematic view of the convection cell and thermal regulation system.

allow for convenient filling of the cell. The lateral walls are made of 2 cm thick blocks of optical quality BK7 glass, whose thermal characteristics can be found, for example, in Koster & Müller (1984) and references therein. The reason for this choice was its extremely low refraction index versus temperature coefficient, two orders of magnitude below that of the fluid under study. The effect of finite size and non-perfectly conducting lateral boundary conditions will be discussed in §2.4. The closure of the cell is accomplished by means of two O-rings, buried in suitable grooves made in the copper plates.

Each copper plate is in contact with an electrical heater and, by means of two aluminium plates, in thermal contact with a thermostated water reservoir that works as a cold source to short the thermal inertia of the system.

The above-described cell is contained in a Plexiglas box with optical-quality glass windows through which the measurements are carried out, and the whole system plus the optics to be described in §2.2 are placed in a vibration-isolated optical table.

The temperature regulation is accomplished with three independent systems that are schematically shown in the block diagram in figure 1. First, there is a thermostatic water bath (Haake model F3K) with a measured temperature stability of 0.025 °C. As stated above the water circulates in two reservoirs in thermal contact with the electrical heaters, the copper plates serving as the cold source. The two heating elements are electrical resistors of 60 Ω and approximately 50 cm^2 area. These electrical heaters are connected to two independent control systems. The temperature in the upper copper plate is controlled by means of a thermistor (Th3) introduced through a hole and in good thermal contact with it. This thermistor is inserted in a branch of an a.c. bridge (T1 stabilizer), excited with the oscillating output of a lock-in amplifier (PAR model 5203) which is also used to detect the unbalance of the bridge, and whose output drives an external voltage-controlled power supply unit that feeds the upper plate heater. The measured long-term stability of the upper plate temperature is ± 0.002 °C.

The last part of the system stabilizes the temperature difference between the two copper plates (ΔT stabilizer). This difference is sensed through two matched

thermistors inserted in both plates (Th1 and Th2). These thermistors are included in a d.c. bridge whose output drives another voltage-controlled power supply that feeds the bottom plate heater. With this system the long-term stability of the temperature difference is better than ± 0.001 °C. The actual temperature difference across the fluid layer has been measured with two calibrated thermistors inserted in both copper plates (Th4 and Th5).

The last d.c. bridge has the salient feature that one of its branches is built around two cascaded digitally controlled potentiometers that allow automatic temperature difference changes by using a microcomputer. In this way the process of control parameter changing is fully automated.

The working fluid is M3 silicone oil for which we have measured the following set of parameters at 25 °C; $\nu = 2.88 \times 10^{-2}$ cm^2 s^{-1}, $\rho = 0.88$ g cm^{-3}, $\alpha = 8.9 \times 10^{-4}$ K^{-1}, $\kappa = 1.05 \times 10^{-3}$ cm^2 s^{-1}, therefore giving $Pr = 27.5$ at $T = 25$ °C. Furthermore we have measured the fluid's relevant optical constants, i.e. the index of refraction $n = 1.395$, and its thermal coefficient $\mathrm{d}n/\mathrm{d}T = 4.6 \times 10^{-4}$ K^{-1}.

Finally the room temperature is maintained stable within 1.5 °C, allowing reasonable stability of all electronics.

2.2. *The scanning technique*

There are several optical techniques that have been used in convection experiments with transparent fluids and which take advantage of the temperature dependence of the index of refraction of the fluid. Examples of these techniques include the focalization images (Pocheau *et al.* 1985; Kolodner *et al.* 1986*b*), interferometric methods (Chu & Goldstein 1973; Berge & Dubois 1979; Koster & Müller 1984), schlieren (Dubois *et al.* 1983) and beam deflection (Giglio, Musazzi & Perini 1981; Arechi, Ciliberto & Rubio 1984). The method used here, that we will explain briefly, is an original improvement of the beam deflection technique and has already been thoroughly described in Ciliberto *et al.* (1985).

The detection system consists of a laser beam that crosses the silicon oil perpendicular to the (X, Z)-plane and is deflected by the thermal gradients inside the fluid layer. For small deviations and supposing the structure of the flow is mainly bidimensional, the deflection angles along x and z are related to the thermal gradients inside the fluid by the following formulae:

$$\theta_x = \frac{\mathrm{d}n}{\mathrm{d}T}\frac{\partial T}{\partial x} l_y; \quad \theta_z = \frac{\mathrm{d}n}{\mathrm{d}T}\frac{\partial T}{\partial z} l_y.$$

The laser beam sweeps the (X, Z)-plane and we can measure the temperature gradient averaged along y as a function of x and z.

In our experimental set-up, shown in figure 2, the sweep is similar to a TV raster scan. The scanning mechanism is built up with two mirrors M_1 and M_2 mounted on two galvanometers, for the x- and z-scan respectively, and the lenses L_1 and L_2, which have the same focal length and are mounted in a confocal configuration to prevent the divergence of the laser beam in the testing region.

The two mirrors M_1 and M_2 are placed very close to each other and their distance from L_2 is equal to the focal length of L_2. With this arrangement the laser beam deflected by the two mirrors reaches the testing region, where the cell is placed, remaining parallel to the optical axis at every position of the two-dimensional sweep, within 3 mrad. This small error is due mainly to the small distance between M_1 and M_2 which makes perfect focusing of both mirrors impossible.

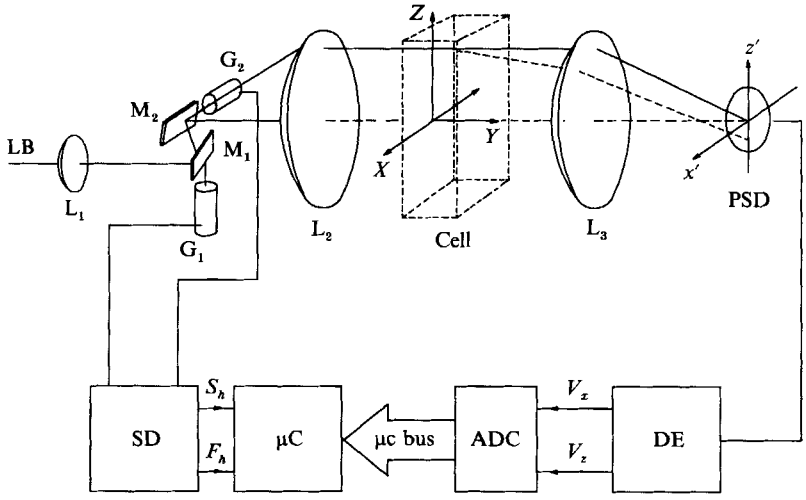

FIGURE 2. Optical set-up. LB laser beam; G_1, G_2 galvanometers; PSD position sensitive detector; DE detector electronics; ADC analog to digital converter; μC microcomputer; SD scanners driver; S_h, F_h synchronization pulses.

The sweeping laser beam, after crossing the cell, is collected by the lens L_3 on the position sensitive detector (PSD) that is placed on the focal plane of this lens. The detector outputs in x and z are sent to specific electronics that amplifies both signals and normalizes them with respect to the total intensity reaching the PSD, therefore compensating for fluctuations in the laser intensity.

The electronics output voltages are proportional to the coordinates of the barycentre of the light distribution on the detector surface, whose position is related to the thermal gradients through the expressions

$$d_x = Fl_y \frac{\mathrm{d}n}{\mathrm{d}T}\frac{\partial T}{\partial x}; \quad d_z = Fl_y \frac{\mathrm{d}n}{\mathrm{d}T}\frac{\partial T}{\partial z},$$

where F is the focal length of L_3. In this way the two components of the temperature gradient may be measured.

The last part of the system includes the data acquisition, based on two 12-bit resolution AD converters, interfaced with a personal computer (Olivetti M-24). This system samples and stores both V_x and V_z signals for each of the horizontal lines. The data acquisition is synchronized with the sweep by sending to the microcomputer the pulses F_h and S_h that mark, respectively, the beginning of the raster scan and the start of every horizontal sweep.

For the measurements that will be reported in §4 the data $(\partial T/\partial x, \partial T/\partial z)$ were taken in frames of 16 horizontal rows of 64 points each. The complete frame is restricted to an effective area of $L_x = 3.6$ cm and $L_z = 0.8$ cm. The spacings between points in the x- and z-directions are 0.06 and 0.056 cm, respectively, both comparable with the laser beam width, 0.07 cm in the measuring region. The size of the frame is smaller than that of the cell because the beam has to be kept a certain distance away from the copper plates and the lateral walls to avoid reflections from them that may yield spurious signals.

The problem of errors has been fully described in Ciliberto *et al.* (1985). We will just note that the overall accuracy of these measurements is about 5% and the sensitivity better than 0.03 °C cm^{-1}, by using the following optical components: Melles-Griot

05 LHR 121 He-Ne laser, General Scanning G120DCM galvanometers, lenses with 30 cm focal length and position sensitive detector, UDT100.

In every run the horizontal scanner was driven at a frequency of 40 Hz allowing us to take a picture of the whole cell in 0.4 s. This time interval compared to the maximum oscillating frequency found in this system (100 mHz), permits the acquisition of more than 15 frames per cycle, yielding a good spatiotemporal characterization of the temperature field in all regimes.

A limitation of the method is the insufficient vertical resolution near the horizontal boundaries, which does not allow a detailed study of the boundary layers in this cell. However, the thermal perturbations detaching from the boundary layers are clearly observed and measured in the reconstructions of the temperature field.

Finally, it is important to point out that the heating produced by the laser beam used to measure the temperature field is completely negligible. The power of the laser was 1 mW and at its optical frequency the absorption coefficient of the silicon oil is very small. Furthermore, a direct test did not show any appreciable change of the behaviour of the fluid from the instant at which the laser was switched on.

2.3. *General procedures and signal processing*

As a general rule, a conveniently averaged frame $T_0(x,z)$ and a sweep $u_0(x)$ at zero ΔT were recorded and automatically subtracted from the actual data to take out of the signal the spurious contributions due to aberrations and unavoidable alignment errors of the optics.

For purposes requiring a high number of samples (e.g. fractal dimension calculation, Fourier spectra, etc.) we have focused our attention on the evolution of a single horizontal scan $u(x,t) = \partial T(x,z_0,t)/\partial x$, measured at 64 points on a horizontal line at height z_0. The length of the line covers the whole horizontal length of the cell because in this case the alignment is less critical than in the bidimensional case. This choice of taking just one horizontal line has an experimental justification. The spatiotemporal dynamics of the system does not depend sensitively on the z-coordinate, except for the absolute amplitude of the dynamical phenomena.

A data file with 4096 complete frames would fill nearly 17 Mbytes of memory yielding unpractical the storage and unfeasible the treatment of such an amount of data. Thus for each time-dependent regime we recorded several frames at selected instants and the $u(x,t)$ for at least 4096 time steps in the periodic and quasi-periodic regimes and 8192 in the chaotic ones.

To better identify the different spatiotemporal regimes we have computed the function $w(x,t) = u(x,t) - \bar{u}(x)$ that accounts for the fluctuations of $u(x,t)$ around the time-averaged pattern $\bar{u}(x)$. The amplitude of u and w are measured in terms of the vertical temperature gradient between the two plates $\Delta T/d$.

We have also computed the spatiotemporal correlation function defined as

$$C(\Delta,\tau) = \int_0^{\frac{1}{2}l_x}\int_0^{T_i} w(x+\Delta,t+\tau)\,w(x,t)\,\mathrm{d}x\,\mathrm{d}t,$$

where T_i is the time interval over which the integral has been computed.

By means of a fast Fourier transform (FFT) algorithm we have calculated frequency Fourier transforms,

$$S(x,f) = \sum_{t=0}^{T_i} u(x,t)\exp(-\mathrm{j}ft),$$

which allows us to know about the spatial distribution of the oscillating frequencies.

We have also computed time-resolved spatial Fourier transforms (TRSFT),

$$\varphi(n,t) = \sum_{x=0}^{l_x} u(x,t)\exp(-\mathrm{j}knx)$$

where $k = 2\pi/l_x$. The Fourier transforms have been computed with a Cooley–Tuckey FFT algorithm upon single scans that contain 64 spatial data points, and the corresponding spectra yield complex amplitudes of the first 32 spatial modes, ranging from $n = 0$ to $n = 31$, which have proved to be enough for the analysis of these structures. By means of these TRSFT we have been able to study the number of modes involved in the dynamics and their relative importance in the time-dependent regimes.

Turning to the problem of characterizing the attractors, the fractal dimension and the metric entropy have been calculated from 8192 samples of $u(x,t)$, allowing therefore the measurement of the spatial dependence of both quantities.

Besides the previously defined parameters that are to be calculated from $u(x,t)$, we can also recover the bidimensional temperature field $T(x,z)$ averaged over Y. To achieve this goal it suffices to integrate the gradient field with the formula

$$T(x,z) = \int_0^x \frac{\partial T(x',z)}{\partial x'}\mathrm{d}x' + \int_0^z \frac{\partial T(0,z')}{\partial z'}\mathrm{d}z'.$$

In this way the temperature field is reconstructed up to a constant factor $T(0,0)$ that cannot be accurately measured because the horizontal thermal boundary layers are not well resolved due to optical alignment problems.

2.4. *Experimental procedure*

The experiment was performed in the following way. We start from zero temperature difference between the two plates, and the frame $T_0(x,z)$ and the sweep $u_0(x)$ at zero gradient are recorded. Then we increase the temperature of the bottom plate up to a maximum difference around $300R_c$. The quasi-steady steps by which the temperature difference has been increased are separated by a sufficient amount of time for the system to relax to a stable state. This time was usually between one and two times the longest horizontal diffusion time τ_h, which in our cell was 1.6×10^4 s. It has also been checked several times that this relaxation time was sufficient to reach a stable state far above threshold. In this way a complete run lasts about three weeks. This type of run was repeated several times to check for the dependence of the attained regimes on the way in which the control parameter was varied.

Finally, we labelled the different regimes found using $r = \Delta T/\Delta T_c$, where ΔT_c is the theoretical critical temperature difference in the limit $\Gamma \gg 1$ and computed using the fluid parameters at 25 °C. This value is $\Delta T_c = 0.059$ °C, 30% lower than the experimentally determined one of 0.084 °C. This small discrepancy deserves a special comment. The influence of finite cell size in the critical Rayleigh number has been theoretically investigated with either conducting (Catton 1970) or insulating lateral boundaries (Catton 1972). Thorough experimental studies are also available in the literature (Stork & Müller 1972, 1975; Walden *et al.* 1987). The general conclusions to be drawn from these studies are: first, the finite size has a stabilizing effect, i.e. it raises the effective critical R; second, for a given cell geometry, insulating lateral walls are destabilizing.

Computing the theoretical critical temperature differences for the geometry of our cell, we obtain $\Delta T_c = 0.089$ °C for the case of insulating lateral walls (Catton 1972;

Walden *et al.* 1987), and $\Delta T_c = 0.124$ °C for the case of conducting walls (Catton 1970; Stork & Müller 1972). In our case the experimental value shows much better agreement with the one obtained for insulating lateral boundaries.

In any case, a mismatch between the thermal conductivities of the fluid and the lateral walls may influence the behaviour of convection near threshold, because of the presence of horizontal temperature gradients. However, in the regimes of interest here, i.e. $\Delta T \gg \Delta T_c$, this mismatch is not relevant because the heat flow is mainly due to convection. Also, the same experiments carried out in a cell with Plexiglas lateral walls did not show any relevant changes in behaviour.

3. Quantitative characterization of spatiotemporal regimes

When studying spatiotemporal problems in Fourier space two main different situations may appear. In the simplest case the dynamics may be ruled by a very small number of spatial modes and the measurement of the amplitudes of these modes may be sufficient for a complete characterization of the system behaviour. This was the case in the previously cited studies of parametrically excited surface waves (Ciliberto & Gollub 1984). Indeed, it was shown that only two spatial modes were relevant and this observation was later theoretically confirmed (Meron & Procaccia 1986).

On the other hand there may be situations in which many spatial modes are involved. This is usually the case in convection experiments in which many spatial modes are excited when the time-dependent regime appears (Ciliberto & Simonelli 1986). In these situations it would be useful to have some tools that would allow quantitative comparisons to be made between different spatiotemporal regimes. In this sense a parameter has already been defined: the so called 'complexity' (Simonelli & Gollub 1988). It roughly evaluates the number of modes involved in the evolution of the system.

Instead, for this purpose of labelling the different structures we have used two other functions defined using the TRSFT. Defining $\psi_n(t) = |\varphi(n,t)|^2$, we have constructed the energy of $u(x,t)$ as

$$E(t) = \sum_{n=0}^{31} \psi_n(t),$$

and we have also defined a 'spectral entropy' function, $\sigma(t)$, as is usually done in the studies of energy spatial distribution in oscillator chains (Livi *et al.* 1985)

$$\sigma(t) = -\frac{1}{\sigma_{\text{eq}}} \sum_{n=0}^{31} p_n(t) \log (p_n(t)),$$

where

$$p_n(t) = \frac{\psi_n(t)}{\sum_{i=0}^{31} \psi_{i(t)}}.$$

In substance, $E(t)$ accounts for the evolution of the total energy of the signal corresponding to the series $u(x,t)$, and the so-called spectral entropy $\sigma(t)$ is, as stated by Livi *et al.* 1985 an equipartition energy indicator. We have normalized $\sigma(t)$ with respect to the equipartition value

$$\sigma_{\text{eq}} = 32 \,(\log (32)/32) = 1.505.$$

With this normalization the values taken by $\sigma(t)$ range from 0, when all the energy is concentrated in only one excited mode, to 1, for equipartition between all modes. Needless to say, for steady behaviour both E and $\sigma(t)$ assume constant values.

Turning to physical space, spatiotemporal convective regimes usually appear in one of two forms: either as localized oscillations or as travelling perturbations. This observation can also be put in a quantitative form by means of the following parameter:

$$\lambda = \frac{1}{2} \frac{|\eta(\tau)|_{\mathrm{pp}}}{\frac{1}{\tau_0} \sum_{\tau=0}^{\tau_0} \eta(\tau)},$$

where pp indicates peak to peak value and

$$\eta(\tau) = \frac{1}{32} \sum_{\Delta=0}^{\frac{1}{2}l_x} [C(\Delta, \tau)]^2.$$

This parameter, λ, vanishes for a travelling wave and is equal to unity when considering a uniform oscillation of a periodic structure. Therefore, it may be considered as a mean to distinguish between travelling and standing waves. It can be applied in this context, provided that the spatiotemporal autocorrelation function is not quickly decaying in space and time.

4. Experimental results

4.1. *Bifurcation scheme and steady temperature fields*

Convection near threshold has already been extensively studied using different approaches in either large or small boxes (see, for instance, Stork & Müller 1972; Dubois & Berge 1978; Kolodner *et al.* 1986*b*; Walden *et al.* 1987). Moreover, as already stated in §1, our main interest is the interrelation between spatial and temporal degrees of freedom in strongly chaotic regimes at moderately high r. Therefore we skip the problem of convection near threshold and go on with the description of the bifurcation scheme in our system.

Analysing the fluid behaviour as a function of r we first find a steady four-roll structure that remain stable up to $r = 80$. Above this threshold the regimes appearing in this system are outlined in table 1. Within the experimental resolution in our up/down scanning procedure (typically of order ΔT_c), the bifurcations to the time-dependent regimes were always found to be supercritical, i.e. no hysteresis was observed.

It is worth saying that, from one run to another, the r-values corresponding to the appearance of the intervals are reproducible within 10%; in addition, the interval length does not change significantly. In contrast, in some regions of r, the behaviour of the system in time-dependent regimes can be different for different runs. For instance, interval I_1 of localized oscillations that do not develop a chaotic evolution is not observed in all runs, interval I_5 shows usually only periodic oscillations, but sometimes we have observed subintervals of quasi-periodic and chaotic behaviour, and, finally, interval I_7 presents a stationary regime in some runs and very small-amplitude localized oscillations in others. These differences depend on the speed with which the temperature gradient was raised and on the sequence of states crossed by the system. In this context, we will focus our attention just on the general characteristic features that we always observe.

Interval	r	Regime	Spatial structure
I_1	80–90	TD†	R4+LO
I_2	90–95	S	R4
I_3	95–130	TD	R5+LO+TW
I_4	130–150	S	R4
I_5	150–182	TD	R4+LO
I_6	182–186	SHO	R4+RW
I_7	186–200	‡	‡
I_8	200–300	TD	R4+LO+TW

† The interval I_1 is not observed in all of the runs.

‡ The interval I_7 presents a stationary regime in some runs and localized oscillations of very small amplitude in others.

TD, time dependent, S, stationary, SHO, Shilnikov-type homoclinic chaos, R4, four-roll structure, LO, localized oscillations, TW, travelling waves.

TABLE 1. Regimes of fluid behaviour as a function of r

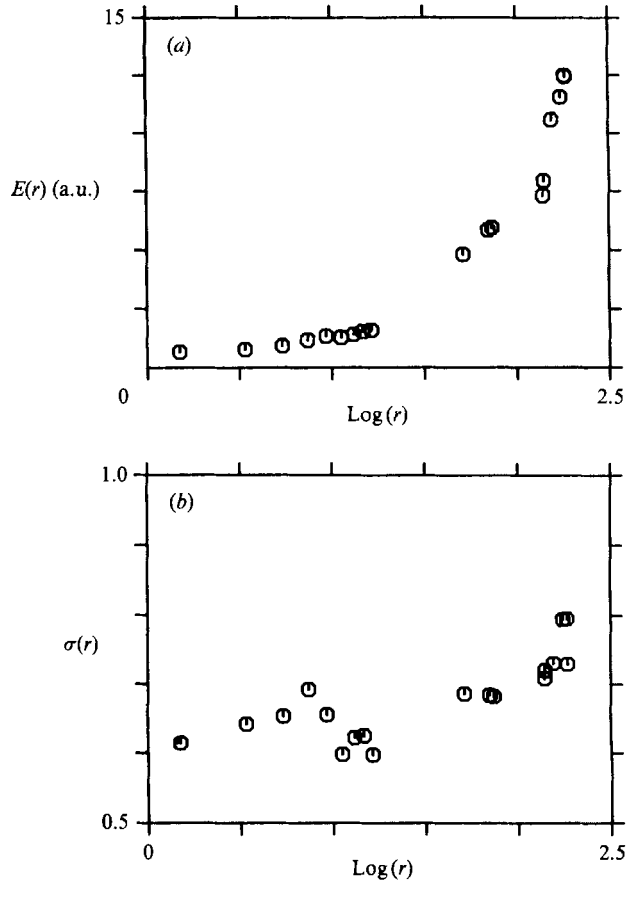

FIGURE 3. (*a*) Time-averaged energy $\overline{E(r)}$, and (*b*) spectral entropy $\overline{\sigma(r)}$ as functions of the reduced temperature r in linear–log scale. (r is represented in a log scale to cover the whole measurement range).

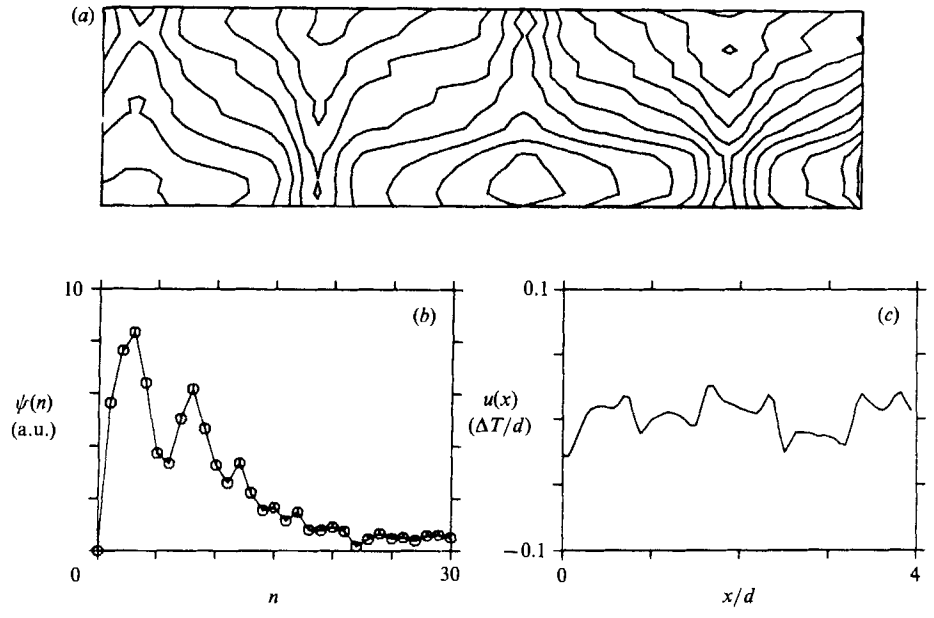

FIGURE 4. Stationary structure at $r = 35$. (*a*) Isotherm map, separation between isotherms is 0.085 °C. (*b*) Spatial Fourier spectrum of $u(x)$. (*c*) Corresponding $u(x)$.

The time-averaged values of the energy $\overline{E(r)}$ and the entropy $\overline{\sigma(r)}$ are reported, as a function of $\log(r)$, in figures 3(*a*) and 3(*b*) respectively. The energy increases roughly linearly with r, while the entropy shows a more complex behaviour. The error in both measurements is smaller than the size of the symbols. As shown in figure 3(*b*) the entropy initially increases up to $r = 7.5$. Above this value it decreases up to $r = 20$, while the energy remains nearly constant, i.e. it is concentrated in a smaller number of modes. This happens because, for these values of r, the characteristic wavelength of the convective structure is a submultiple of the cell length.

A stationary structure is depicted in figure 4(*a*), at $r = 35$, where the isotherms are shown. The expected four-roll structure is immediately recognized, although owing to the aforementioned alignment problems the extreme right ascending current has been lost in the picture. The separation between isotherms is 0.085 °C.

The horizontal temperature gradient at the middle plane of the cell, i.e. $u(x)$, is shown in figure 4(*c*), and its spatial Fourier spectrum is plotted in figure 4(*b*).

We report also the highest stationary spatial structure in our system that was found at $r = 146$, corresponding to interval I_4 in table 1. In figure 5(*a*) we have plotted the temperature field with a separation between isotherms of 0.66 °C; we also show its corresponding $u(x)$ and the spatial spectrum $\phi(n)$ of $u(x)$ in figures 5(*c*) and 5(*b*) respectively. In figure 5(*a*) another four-roll structure can be recognized, although the extreme left ascending current is not visible in this level plot. The whole structure resembles very much that in figure 4(*a*) with some minor differences, but upon comparing the horizontal gradients at middle height these differences become more clear. First, for $r = 146$, the division of the convective flow into four main rolls is reinforced (see the sharp changes of sign of $u(x)$ in the boundaries between rolls). Second, $u(x)$ is more irregular in figure 5(*c*), which reveals the increasing importance of higher harmonics in the flow configuration.

These points may be better seen by comparing both spatial spectra (figures 4*b* and

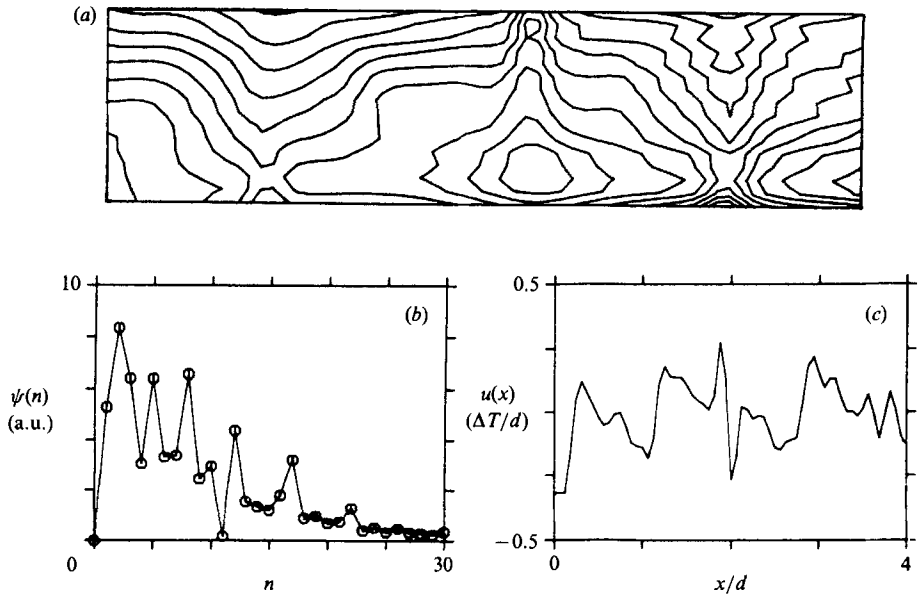

FIGURE 5. Stationary structure at $r = 146$. (*a*) Isotherm map, separation between isotherms is 0.66 °C. (*b*) Spatial Fourier spectrum of $u(x)$. (*c*). Corresponding $u(x)$.

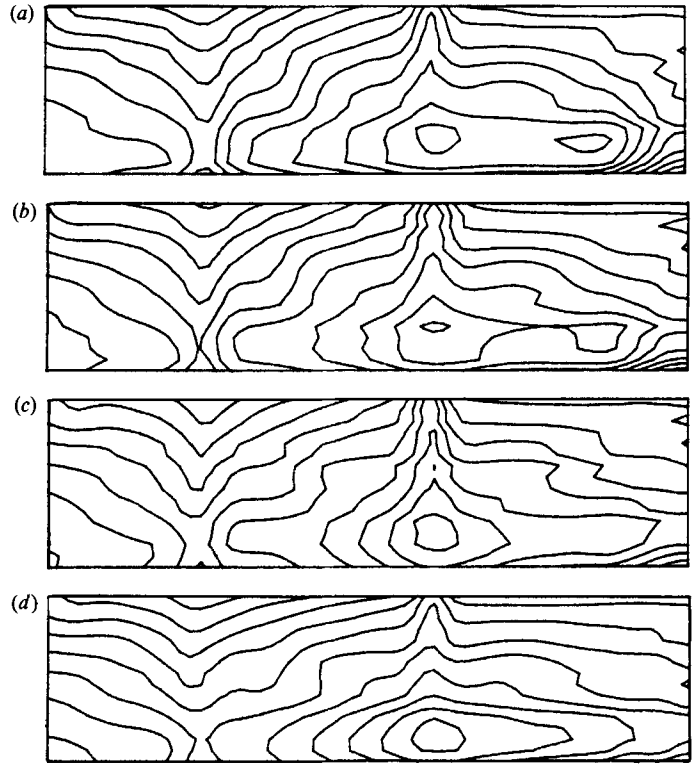

FIGURE 6. Time-dependent temperature field for a localized monoperiodic regime with frequency $f = 78$ mHz ($r = 89.5$). Interval between pictures is 3.2 s; separation between isotherms is 0.4 °C.

5*b*). In figure 4(*b*) the most important spatial modes are $n = 3$ and $n = 8$. In figure 5(*b*), the most important mode is $n = 2$, while modes 3, 5 and 8 have roughly equal amplitudes. In this case beating between $n = 2$ and the harmonics of mode 5 can be recognized up to $n = 22$.

The main wavelength of a convective structure near threshold is roughly $2d$, so in our cell ($\Gamma = 4$) we should have a four-roll structure; therefore the main peak in the spatial spectrum should be $n = 2$. However, owing to the dependence of q on r, the characteristic wavelength of the spatial structure may not be an integer submultiple of the cell horizontal length. So in this case the main peak may change its position from $n = 2$ to $n = 3$, owing to the perturbation introduced by the finite size of the cell.

The values obtained for the energy and the entropy of both structures in figures 4 and 5, are $E = 2.5$, $\sigma = 0.6$, for $r = 35$, and $E = 7.9$, $\sigma = 0.72$, for $r = 146$. The values of E do not add information in this case, being higher at higher r as expected, but σ confirms the conjecture that in the second structure the energy is distributed among a number of modes higher than in the first one.

4.2. *Periodic and chaotic behaviour: localized oscillations and travelling waves*

Some aspects of the first time-dependent stages, mainly concerning the temporal features, have already been reported by Ciliberto & Rubio (1987*a*, *b*). In this paper we will focus our attention on some spatiotemporal features that remained unclear in previous studies.

To understand the nature of the oscillators we have plotted in figures 6 and 7 the evolution of the temperature field in the time-dependent regimes corresponding to the intervals I_1 and I_3 in table 1.

Figure 6(*a–d*) is at $r = 89.5$, a value at which a monoperiodic oscillating regime is present, and they have been recorded with a delay time between pictures of 3.2 s. The whole series plotted corresponds to one period of the oscillation (the following picture in the sequence would be equal to figure 6*a*), and the separation between isotherms is 0.4 °C.

This oscillator can be identified as a hot drop that is periodically formed in the lower-right part of the cell. The main characteristic of this drop is that its position does not change with time, i.e. only its volume is time-dependent. Moreover the temperature field is affected only in the right part of the cell, the left one remaining almost unchanged. In this sense this is a localized oscillator.

In figure 7(*a–f*), at $r = 128.5$ with a delay of 2.4 s between pictures, we have plotted the evolution of the temperature field corresponding to interval I_3, with a separation between isotherms of 0.58 °C. In this case the behaviour, although corresponding to a monoperiodic oscillator too, is more complex. In this case the whole structure of the temperature distribution is changing with time. The analysis of $u(x, t)$ will clearly show the existence of travelling perturbations for this type of globally time-dependent temperature field.

As representative examples we show figures 8 and 9, at different r-values from figures 6 and 7, and this selection of r-values deserves a brief comment. Although the localized (respectively global) time-dependence of $T(x, z)$ in figure 6 (respectively figure 7) is also shown for the r-values corresponding to figure 9 (respectively figure 8), we have selected these r-values for figures 8 and 9 because they are closer to the regimes to be discussed in §4.3. Conversely, for the images of the whole temperature field, we have chosen lower r-values because at higher r-values $T(x, z)$ is more complex and the plots would be less illustrative at first sight.

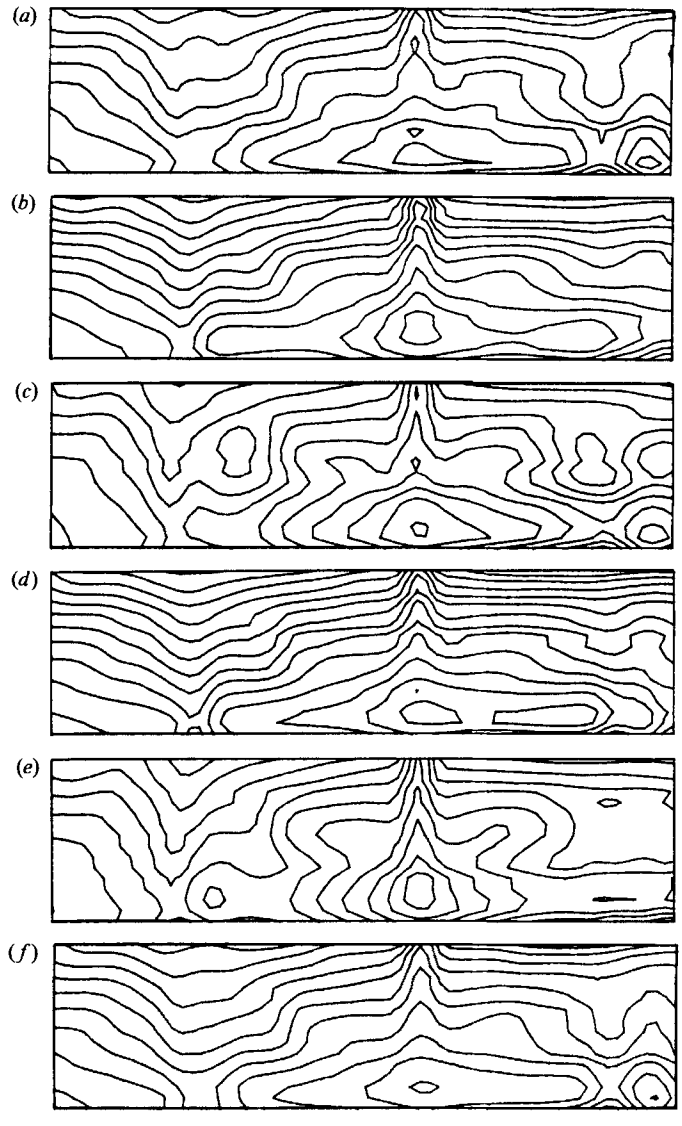

FIGURE 7. Time-dependent temperature field for a travelling wave monoperiodic regime; frequency $f = 83.3$ mHz ($r = 128.5$). Interval between pictures is 2.4 s; separation between isotherms is 0.58 °C.

In figure 8 we have plotted four different representations of the dynamics for a state equivalent to that in figure 7 at $r = 130$. These representations are respectively the evolution of $u(x,t)$ (in figure 8*a*), its time-dependent component $w(x,t)$ (in figure 8*b*), the spatiotemporal correlation function of $w(x,t)$, i.e. $C(\Delta,\tau)$ (in figure 8*c*) and finally the position of the maxima of $C(\Delta,\tau)$ as a function of τ (in figure 8*d*).

Conversely, in figure 9 we have plotted the same functions as in figure 8 measured at $r = 174.5$, which corresponds to a localized state equivalent to that shown in figure 6.

Certainly the difference appears more clear when comparing figures 8(*c*) with 9(*c*), and 8(*d*) with 9(*d*). In figure 9(*c*) the space–time correlation function can be decomposed to a product of two functions. One depends only on the spatial

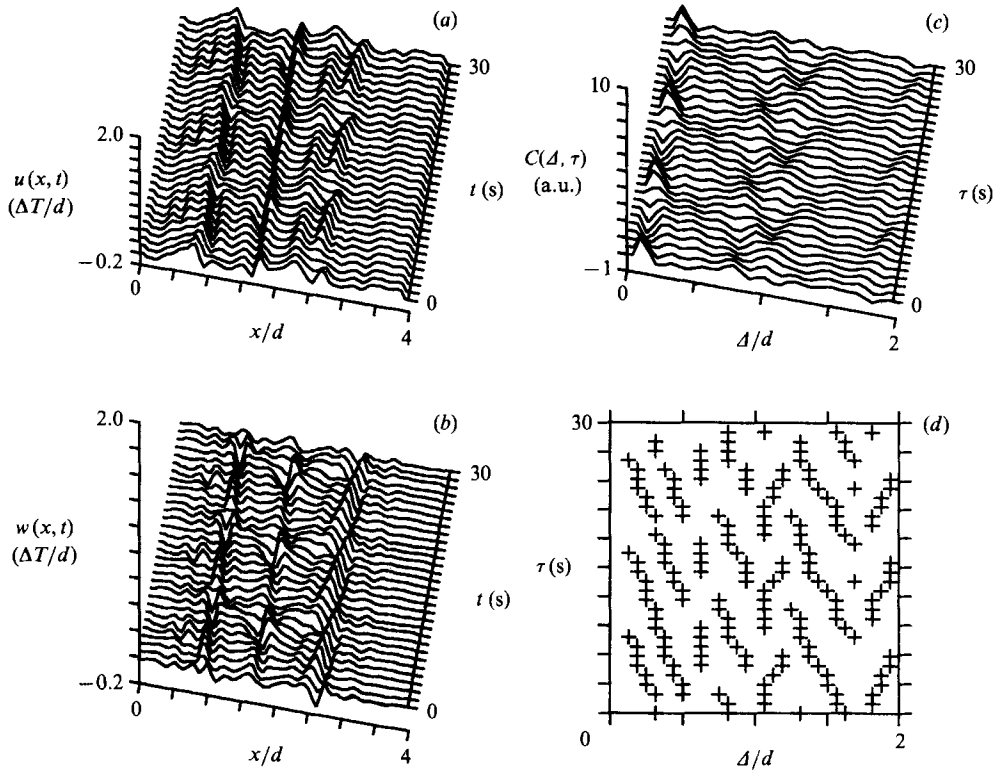

FIGURE 8. Travelling wave behaviour at $r = 130$. Space–time evolution of (*a*) $u(x,t)$ and (*b*) $w(x,t)$; (*c*) corresponding $C(\Delta,\tau)$. (*d*) Time evolution of the positions of the maxima of C (crosses).

coordinate while the other is periodic in time. This decomposition means that the thermal oscillation is a standing wave. Furthermore, as it is possible to see in figure 9(*b*), it is localized in the left side of the cell. This is also confirmed by the evolution of the maxima in figure 9(*d*) which always stay at a fixed position as time passes, and more quantitatively by the localization parameter. In fact we have $\lambda = 0.91$ for the localized oscillation at $r = 174.5$, and $\lambda = 0.24$ for the travelling perturbation at $r = 130$. Figure 8(*c*) is more complex because it also shows the presence of some propagating perturbation. This is quite clear in figure 8(*d*), where the maxima of $C(\Delta,\tau)$ reveal a certain travelling behaviour. This travelling behaviour appears also at higher values of r as may be seen in figure 10(*a–d*) taken at $r = 260$, where the same functions as in figures 8 and 9 have been plotted.

It is useful to point out that in both cases the character of the spatiotemporal behaviour is seen much better on the correlation function than in the actual experimental signal $u(x,t)$ (figures 8*a* and 9*a*), or its time-depending part $w(x,t)$ (figures 8*b* and 9*b*).

The observed velocities V of propagation of the maxima of $C(\Delta,\tau)$, range between 0.03 and 0.08 cm/s, consistent with the velocity scale $\nu/d = 0.03$ cm/s. We did not find any law relating V either to r or to the frequency of oscillation, but it slightly depends on the z-coordinate where $u(x,t)$ has been measured. It is larger near the top and the bottom of the cell than in the centre.

It is important to remark that we have not found a general relationship between localized or travelling perturbations and the associated time evolution, either

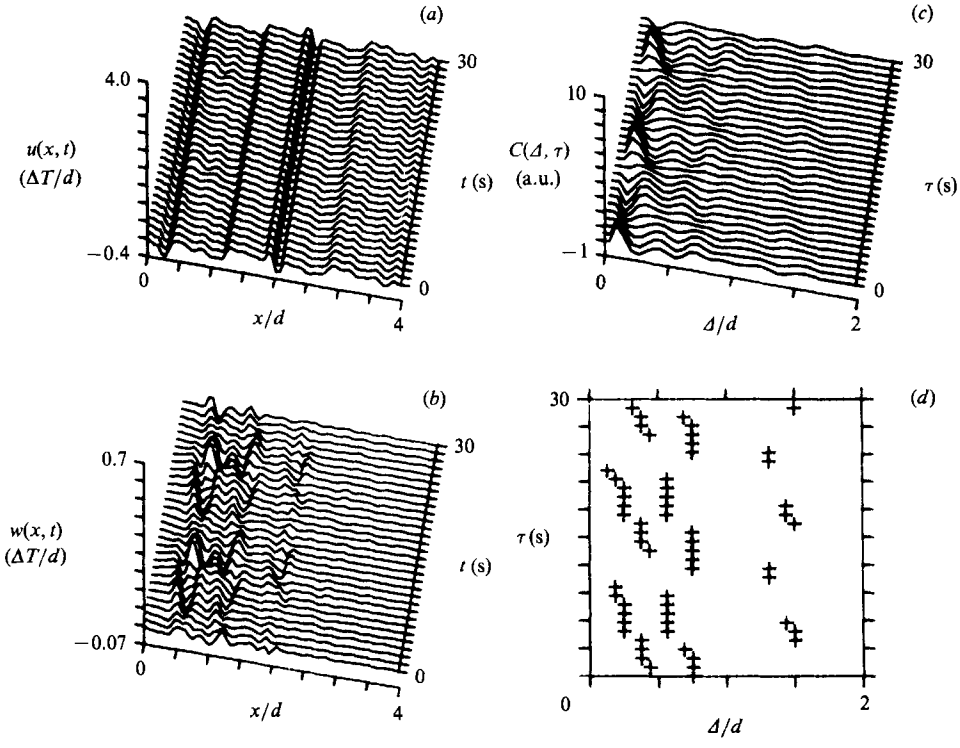

FIGURE 9. Localized oscillations at $r = 174.5$. Space–time evolution of (*a*) $u(x,t)$ and (*b*) $w(x,t)$; (*c*) corresponding $C(\Delta,\tau)$. (*d*) Time evolution of the positions of the maxima of C (crosses).

periodic or chaotic. More specifically, inside the interval I_6 reported in table 1, we have found some special cases of transition between localized oscillation and travelling waves that have an intrinsic interest due to some special features that will be described in §4.3. This type of transition corresponds to an homoclinic orbit, probably of Shilnikov type (Guckenheimer & Holmes 1983).

4.3. *Transition between localized oscillations and travelling waves*

The transition occurs at $r_0 = 182$. The spatiotemporal regime prior to this bifurcation can be identified as a localized one such as that shown in figure 9(*a–d*).

Upon increasing r over the critical value r_0, there is a marked change in the spatiotemporal evolution of the system. For $r < r_0$, the energy and the local temperature gradient at any point of the cell show smooth time-dependence, irrespective of the actual regime being periodic or chaotic.

At $r = 184$, the time evolution of the energy $E(t)$ is shown in figure 11(*a*). A detailed analysis of this signal reveals that there are regular oscillatory periods that are suddenly interrupted by randomly distributed energy pulses that last about 200 s. During these pulses, which we will call bursts in the following, the energy shows mean value changes larger than the oscillation amplitude in the regular periods. This type of temporal behaviour, which is observed in a global variable such as the energy, is also present in the evolution of temperature gradient in any position of the cell.

A closer view of the so-called 'regular periods' shows the existence of two frequencies, with values $f_1 = 15$ mHz, and $f_2 = 168$ mHz. This evolution can be interpreted in the sense that the behaviour of the system in this region of parameter

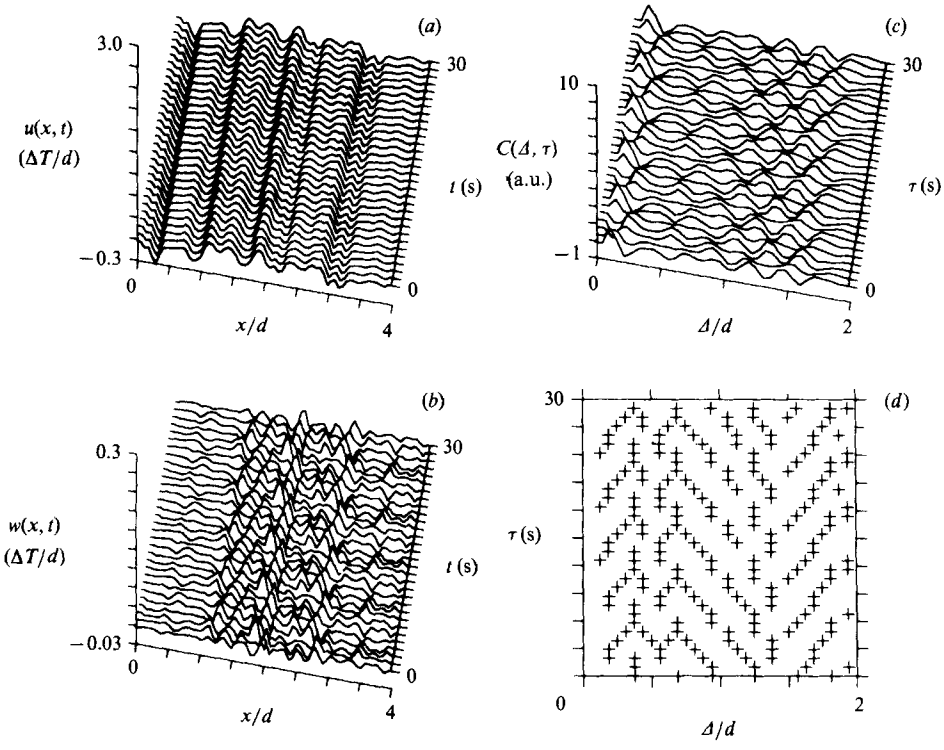

FIGURE 10. Travelling wave behaviour at $r = 260$. Space–time evolution of (*a*) $u(x,t)$ and (*b*) $w(x,t)$; (*c*) corresponding $C(\Delta,\tau)$. (*d*) Time evolution of the positions of the maxima of C (crosses).

space is ruled by five main degrees of freedom. Four degrees of freedom account for the two couples of complex-conjugate eigenvalues with negative real part corresponding to the two damped oscillating modes associated with the frequencies f_1 and f_2. The last degree of freedom corresponds to the positive real eigenvalue that allows for the bursting behaviour. A fractal dimension calculation for this regime gives further support to this interpretation yielding a value of 5.2 ± 0.1.

This type of evolution is characteristic of Shilnikov-type homoclinic chaos that has been observed in numerical integration of simple models of nonlinear partial differential equations (Hyman & Nicolaenko 1986), and in Rayleigh–Bénard convection experiments in a cell with $\Gamma = 3$ (A. Sano 1988, private communication). A behaviour similar to the Shilnikov type has been also reported in a model for large-scale flow in Rayleigh–Bénard convection (Howard & Krishnamurti 1986). The appearance of a large-scale flow might be the reason for the existence of our travelling perturbation. This conjecture is reinforced by recent results (Linz *et al.* 1988) that show a possible relationship between travelling wave behaviour and large-scale lateral mean flow in a model of convection in a binary mixture.

We have carefully compared the spatiotemporal characteristics of the numerical solutions of the above-mentioned equations (Hyman & Nicolaenko 1986) with those found in our experiment.

Several of these spatiotemporal characteristics could be checked in our system. Indeed in these mathematical models the appearance of the Shilnikov-type chaos

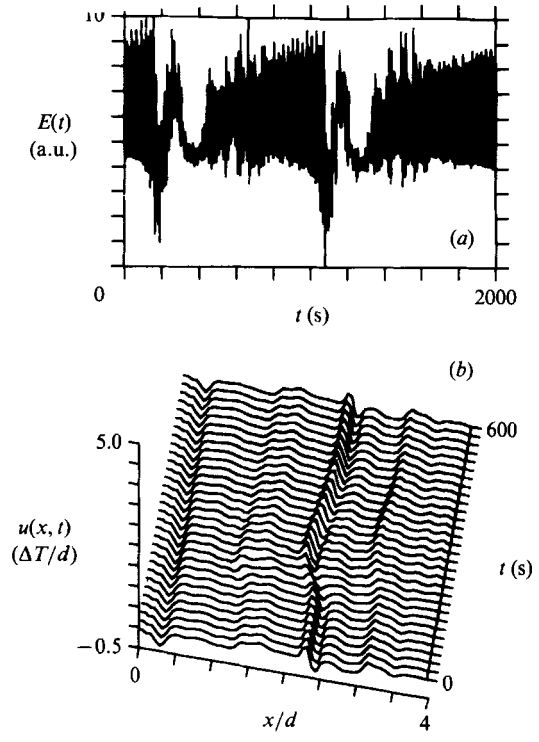

FIGURE 11. Transition between localized oscillations and travelling waves at $r = 184$. (*a*) Time evolution of the energy $E(t)$. (*b*) Space–time evolution $u(x,t)$ averaged over four periods of the fast oscillations.

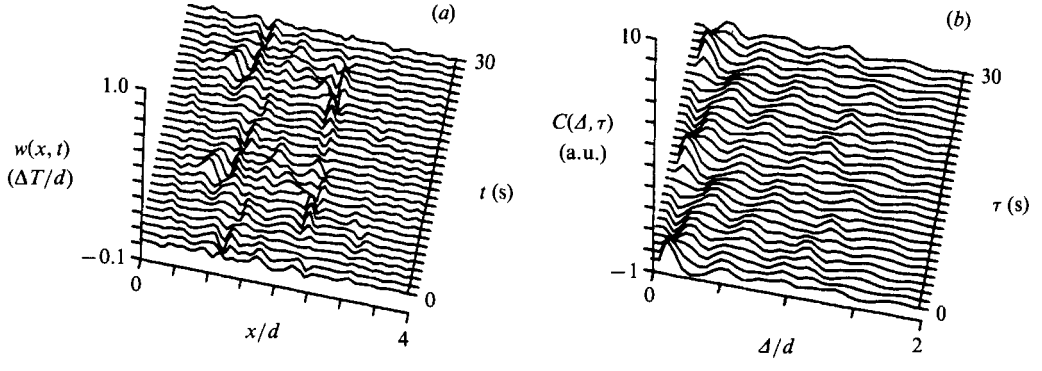

FIGURE 12. (*a*) Space–time evolution of $w(x,t)$ recorded during the laminar period of the regime shown in figure 11. (*b*) Corresponding correlation function $C(\Delta,\tau)$.

coincides with a change in the spatial distribution of the oscillators; before the bifurcation, the oscillators are localized while after the bifurcation travelling waves are present.

Moreover, the bursts are associated with major changes in the spatial structure of the solutions. These bursts are found to be coincident with the re-emergence of the stationary spatial structure existing just prior to this transition. Finally, even-wavenumber spatial modes evolve in counter phase with respect to the odd ones.

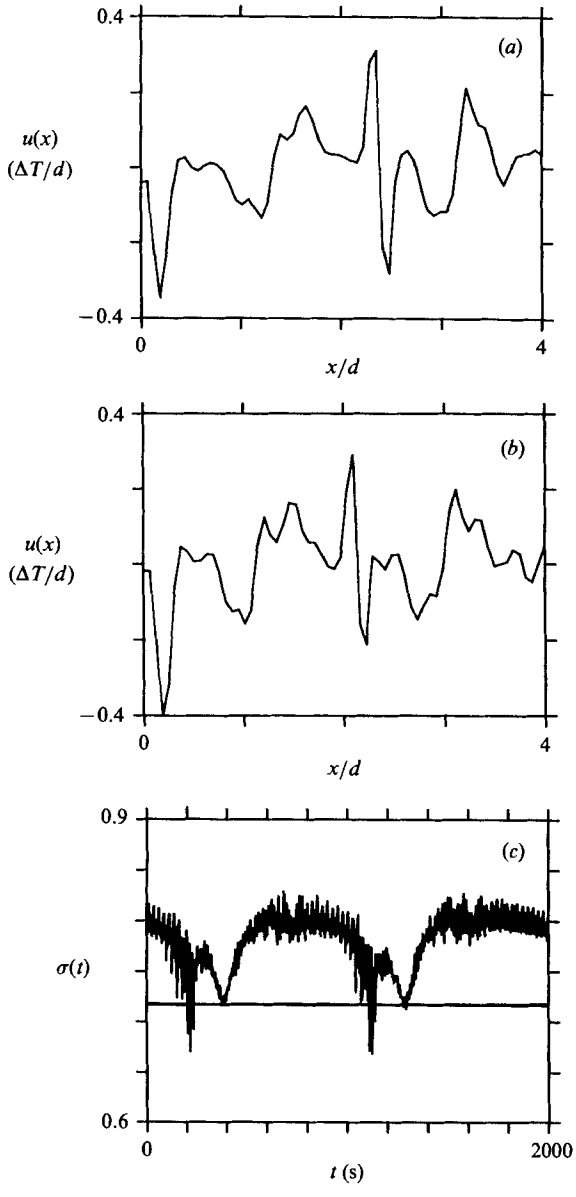

FIGURE 13. Time-averaged spatial structures at $r = 184$, (*a*) during the laminar period, (*b*) during the burst. (*c*) Time evolution of the entropy at $r = 184$; the horizontal line corresponds to the value of the entropy for the structure in figure 5(*c*) ($r = 146$).

Turning back to our experimental results, some of these spatiotemporal features can be unambiguously seen in figures 11(*b*) and 12(*a*, *b*), corresponding to a value of $r = 184$.

In figure 11(*b*) we have plotted the evolution of $u(x, t)$ averaged over four periods of the fast oscillation. During the burst there is a large structure change that corresponds to a quick shift of the main current to a more centred position. In the following regular period, this current slowly returns to its original position, until the next burst takes place.

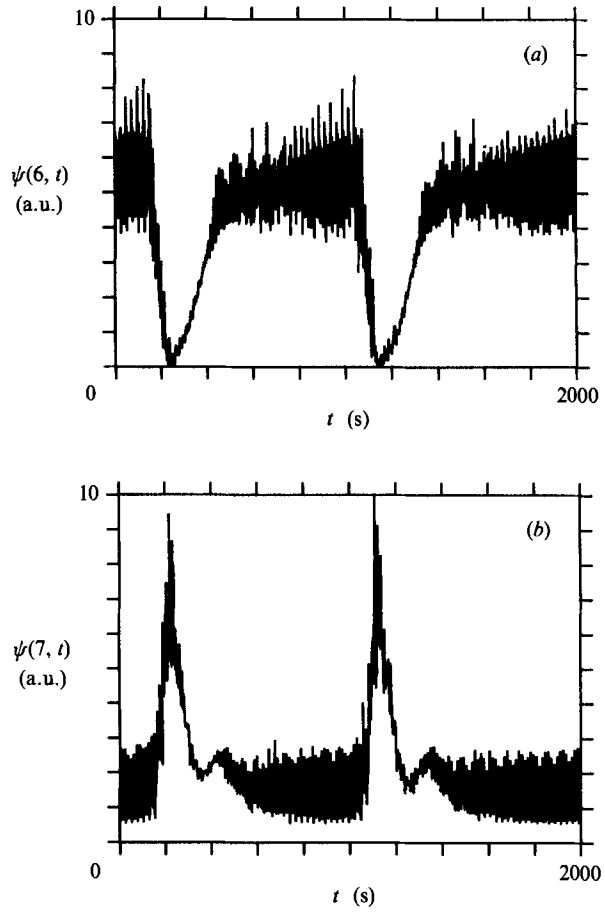

FIGURE 14. Time evolution of the amplitudes of the spatial modes (*a*) $n = 6$, (*b*) $n = 7$ at $r = 184$.

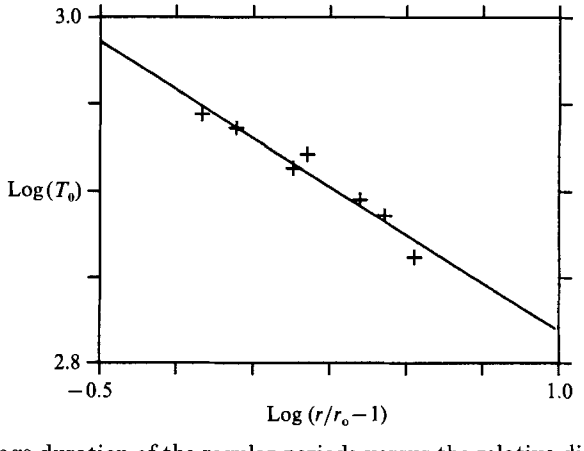

FIGURE 15. Average duration of the regular periods versus the relative distance to the bifurcation. Experimental points (crosses) and least-squares fit (solid line).

In figure 12(*a*) we show $w(x,t)$ recorded during a laminar period of the regime depicted in figure 11(*a*). Its spatiotemporal correlation function is reported in figure 12(*b*). The presence of a travelling perturbation can be clearly seen in the correlation function, and therefore a transition from localized oscillations to a travelling wave behaviour has taken place.

An analysis of the spatial structure is carried out in figure 13(*a–c*), where we have shown two relevant time-averaged spatial structures. Figures 13(*a*) and 13(*b*) correspond to the regular and bursting parts of the evolution in figure 11(*a*) respectively. The shift of the central current already described in figure 11(*b*) is seen once again. A strong similarity can be appreciated between figures 13(*b*) and 5(*c*), which, as may be recalled, is the stationary spatial structure existing just prior to the time-dependent regime leading to this transition ($r = 146$).

This check of the similarity between both structures can be performed in a quantitative way using the previously defined spectral entropy. In figure 13(*c*) we show the evolution of this quantity corresponding to figure 11(*a*). The straight line is drawn at the entropy value of the stationary spatial structure in figure 5(*c*). In the bursting region the spectral entropy of the system returns to the value corresponding to the stationary structure. Moreover we found that during the burst there is a large exchange of energy between odd and even spatial modes; this fact can be appreciated in figures 14(*a*) and 14(*b*), where the amplitudes of modes 6 and 7 are shown as a function of time.

Finally, the average duration of the regular periods shows a power-law dependence on the relative distance to the bifurcation. The results are plotted in figure 15, where the crosses are the experimental points and the continuous line corresponds to a least-squares fit that yields the following relation:

$$T_0 = 850(r - r_0)^{-0.11}.$$

The theoretical behaviour to be expected for T_0 very close to the bifurcation point is of exponential type. However, slightly beyond this critical point, a power-law decay with an exponent close to 0.1 has been found in the above-mentioned numerical simulations (B. Nicolaenko private communication). Nevertheless, this may well be a coincidence, for no universality is to be expected in this exponent.

5. Conclusions

5.1. *Main results*

We summarize here the major results of this investigation:

1. We extend previous experimental work on Rayleigh–Bénard convection in small boxes to the study of spatio-temporal regimes.

2. We use a beam deflection scanning technique that allows a complete reconstruction of the temperature field integrated along the roll axis (figures 6 and 7). However, owing to the limited vertical resolution near the horizontal boundaries some relevant physical mechanisms may be missed.

3. By studying the spatio-temporal autocorrelation function of a component of the temperature gradient we identify different structures as being localized or travelling (figures 8 and 9). We also introduce a parameter that accounts for the degree of localization of the spatio-temporal regime.

4. The use of time-resolved spatial Fourier analysis allows us to define an energy and a spectral entropy that are used to make quantitative comparisons between different structures (figures 3 and 13).

5. A transition between localized oscillations and travelling wave regimes has been carefully studied. We show that this transition has many of the properties usually associated with a Shilnikov-type homoclinic chaos (figures 11, 14 and 15) as in Kuramoto-type equations.

5.2. *Discussion*

One novel feature of this investigation is the direct measurement of the temperature field integrated along the roll axis. The beam deflection scanning technique proves to be very useful in this context because the measurement time is much shorter than the characteristic times involved in the dynamics of the convective system. The only important restriction is that the flow configuration should not be strongly three-dimensional.

Moreover, many applications can be imagined. When detection by transmission is needed, the technique reveals the optical disuniformity fields due either to the shape of the object under investigation or to refraction index gradients, regardless of origin. But it can be set up also in a reflection configuration and therefore may be used to detect surface deformations (e.g. Marangoni convection).

The convective spatial structure in small boxes has usually been thought to be frozen by the strong effect of the cell walls. Here, however, we have shown that travelling perturbations can be found, as well as localized ones, for high values of the control parameter r. Furthermore, in such a small cell it has been reported (Ciliberto 1987) that the chaotic behaviour of the system is not uniform; the fractal dimension and metric entropy depend on spatial coordinates. This dependence is stronger when the oscillators are localized. In this case it has been found that the fractal dimension changes from 2.5 to more than 5 from one side of the cell to the other.

The scenario in which these travelling and standing waves appear is very similar to that found in numerical simulations of a Kuramoto-type equation (Nicolaenko 1987) recently derived for a compressible solar convective layer zone (Depasier & Spiegel 1981; Poyet 1983; Depassier 1984). Although our results are only in qualitative agreement with those of Nicolaenko it is tempting to think that a model similar to the above-cited ones may rule the dynamics of our system.

Physical explanations for some features, such as critical ΔT, spatial structure, changes in spatial mode distribution, energy and entropy have been given within the frame of classical results on convection. Unfortunately, when turning to the time-dependent behaviour few explanations can be outlined. For fluids with Prandtl number like ours the time-dependent behaviour is caused by boundary-layer instabilities, and we are not aware of any theoretical or numerical study that could rigorously apply to our system and with which we could compare our data. We certainly do not have explanations for the fact of the Shilnikov-type transition being associated with the change in spatio-temporal behaviour, but this is also true for the simplified models with which we have carried out the comparison. We believe that a detailed understanding of this highly nonlinear phenomenon is far beyond the limits of our present knowledge.

Finally, the introduction into this field of tools developed in statistical mechanics, such as the energy and spectral entropy, seems to be very promising. In a very recent example Rayleigh–Bénard convection has been studied in an annulus (Ciliberto & Bigazzi 1988). The use of statistical mechanics methods has allowed the transition to spatiotemporal intermittency to be characterized as having many of the properties of a phase transition.

The results reported here are limited to a moderately high-Prandtl-number fluid

($Pr = 30$) and small-aspect-ratio cell. For future work these studies should be extended to other Prandtl numbers and larger-aspect-ratio cells. This last experimental condition yields a physical system more manageable from the theoretical point of view and we believe that it might allow for more quantitative comparisons with numerical simulations.

We acknowledge F. T. Arecchi, P. Coullet, F. Simonelli and B. Nicolaenko for fruitful discussions and S. Acciai, S. Euzzor, S. Mascalchi, P. Poggi and A. Tenani or efficient technical assistance. We also acknowledge one of the referees for very useful comments. This work has been partially supported by Gruppo Nazionale di Struttura della Materia.

REFERENCES

AHLERS, G., CANNELL, D. S. & STEINBERG, V. 1985 Time dependence of flow patterns near the convective threshold in a cylindrical container. *Phys. Rev. Lett.* **54**, 1373–1376.

ARECCHI, F. T., CILIBERTO, S. & RUBIO, M. A. 1984 Oscillations and chaos on the free surface of a heated fluid. *Il Nuovo Cimento* **3D**, 793–802.

BADII, R. & POLITI, A. 1985 Statistical description of chaotic attractors: the dimension function. *J. Statist. Phys.* **40**, 725–750.

BERGE, P. & DUBOIS, M. 1989 Study of unsteady convection through simultaneous velocity and interferometric measurements. *J. Phys. Lett. Paris* **40**, L505–L509.

BISHOP, A. R., FESSER, K., LOMDHAL, P. S., KERR, W. C., WILLIAMS, M. B. & TRULLINGER, S. E. 1983 Coherent spatial structure versus time chaos in a perturbed sine-Gordon system. *Phys. Rev. Lett.* **50**, 1095–1098.

BOLTON, E. W., BUSSE, F. H. & CLEVER, R. M. 1986 Oscillatory instabilities of convection rolls at intermediate Prandtl numbers. *J. Fluid Mech.* **164**, 469–485.

BUSSE, F. H. 1987 Non linear properties of thermal convection. *Rep. Prog. Phys.* **41**, 1929–1967.

BUSSE, F. H. & WHITEHEAD, J. A. 1971 Instabilities of convection rolls in a high Prandtl number fluid. *J. Fluid Mech.* **47**, 305–320.

BUZYNA, G., PFEFFER, R. L. & JUNG, R. 1984 Transition to geostrophic turbulence in a rotating differentially heated annulus of fluid. *J. Fluid Mech.* **145**, 377–403.

CATTON I. 1970 Convection in a closed rectangular region: the onset of motion. *Trans. ASME* C: *J. Heat Transfer* **92**, 186–188.

CATTON, I. 1972 The effect of insulating vertical walls on the onset of motion in a fluid heated from below. *J. Heat Mass Transfer* **15**, 665–672.

CHANDRASEKHAR, S. 1961 *Hydrodynamic and Hydromagnetic Stability*. Dover.

CHATE, H. & MANNEVILLE, P. 1987 Transition to turbulence via spatiotemporal intermittency. *Phys. Rev. Lett.* **58**, 112–115.

CHU, T. Y. & GOLDSTEIN, R. J. 1973 Turbulent convection in a horizontal layer of water. *J. Fluid Mech.* **60**, 141–159.

CILIBERTO S. 1987 Fractal dimension and metric entropy in extended systems. *Europhys. Lett.* **4**, 685–690.

CILIBERTO, S. & BIGAZZI, P. 1988 Spatiotemporal intermittency in Rayleigh–Bénard convection. *Phys. Rev. Lett.* **60**, 286–289.

CILIBERTO, S., FRANCINI, F. & SIMONELLI, F. 1985 Real time measurements of optical disuniformity fields. *Optics Commun.* **54**, 251–256.

CILIBERTO, S. & GOLLUB, J. P. 1984 Pattern competition leads to chaos. *Phys. Rev. Lett.* **52**, 922–925.

CILIBERTO, S. & GOLLUB, J. P. 1985 Chaotic mode competition in parametrically forced surface waves. *J. Fluid Mech.* **158**, 381–398.

CILIBERTO, S. & RUBIO, M. A. 1987*a* Local oscillations, travelling waves and chaos in Rayleigh–Bénard convection. *Phys. Rev. Lett.* **58**, 2652–2655.

CILIBERTO, S. & RUBIO, M. A. 1987*b* Chaos and order in the temperature field of Rayleigh-Bénard convection. *Physica Scripta* **36**, 920–926.

CILIBERTO, S. & SIMONELLI, F. 1986 Spatial structure of temporal chaos in Rayleigh–Bénard convection. *Europhys. Lett.* **2**, 285–290.

CURRY, J., HERRING, J., LONCARIC, J. & ORSZAG, S. A. 1984 Order and disorder in two- and three-dimensional Bénard convection. *J. Fluid Mech.* **147**, 1–38.

DEPASSIER M. C. 1984 A note on the free boundary conditions in Rayleigh–Bénard convection between insulating boundaries. *Phys. Lett.* **102A**, 359–361.

DEPASSIER, M. C. & SPIEGEL, E. A. 1981 The large-scale structure of compressible convection. *Astr. J.* **86**, 496–512.

DUBOIS, M. & BERGE, P. 1988 Experimental study of the velocity field in Rayleigh–Bénard convection. *J. Fluid Mech.* **85**, 641–653.

DUBOIS, M. & BERGE, P. 1981 Instabilities de couche limite dans un fluide en convection: evolution vers la turbulence. *J. Phys. Paris* **42**, 167–174.

DUBOIS, M., RUBIO, M. A. & BERGE, P. 1983 Experimental evidence of intermittencies associated with a subharmonic bifurcation. *Phys. Rev. Lett.* **51**, 1446–1449.

FARMER, J. D., OTT, E. & YORKE, J. A. 1983 The dimension of chaotic attractors. *Physica* **7D**, 153–180.

GIGLIO, M., MUSAZZI, S. & PERINI, U. 1981 Transition to chaotic behaviour via a reproducible sequence of period doubling bifurcations. *Phys. Rev. Lett.* **47**, 243–246.

GIGLIO, M., MUSAZZI, S. & PERINI, U. 1984 Low dimensionality turbulent convection. *Phys. Rev. Lett.* **53**, 2402–2404.

GOLLUB, J. P. & BENSON, S. V. 1980 Many routes to turbulent convection. *J. Fluid Mech.* **100**, 449–470.

GOLLUB, J. P. & MCCARRIER, A. R. 1982 Convection patterns in Fourier space. *Phys. Rev.* A **26**, 3470–3476.

GRASSBERGER, P. & PROCACCIA, I. 1983 Characterization of strange attractors. *Phys. Rev. Lett.* **50**, 346–349.

GUCKENHEIMER, J. & BUZYNA, G. 1983 Dimension measurements for geostrophic turbulence. *Phys. Rev. Lett.* **51**, 1438–1441.

GUCKENHEIMER, J. & HOLMES, T. 1983 *Nonlinear Oscillations, Dynamical Systems and Bifurcations of Vector Fields.* Springer.

HEUTMAKER, M. S., FRAENKEL, P. N. & GOLLUB, J. P. 1985 Convection patterns: time evolution of the wave-vector field. *Phys. Rev. Lett.* **54**, 1369–1372.

HOWARD, L. N. & KRISHNAMURTI, R. 1986 Large-scale flow in turbulent convection: a mathematical model. *J. Fluid Mech.* **170**, 385–410.

HYMAN, J. M. & NICOLAENKO, B. 1986 The Kuramoto–Sivashinski equation: a bridge between PDE's and dynamical systems. *Physica* **18D**, 113–126.

KANEKO, K. 1985 Spatiotemporal intermittency in coupled map lattices. *Prog. Theor. Phys.* **74**, 1033–1944.

KOLODNER, P., PASSNER, A., SURKO, C. M. & WALDEN, R. W. 1986*a* Onset of oscillatory convection in a binary fluid mixture. *Phys. Rev. Lett.* **56**, 2621–2624.

KOLODNER, P., WALDEN, R. W., PASSNER, A. & SURKO, C. M. 1986*b* Rayleigh–Bénard convection in an intermediate-aspect-ratio rectangular container. *J. Fluid Mech.* **163**, 195–226.

KOSTER, J. N. & MÜLLER, U. 1984 Oscillatory convection in vertical slots. *J. Fluid Mech.* **139**, 363–390.

KRISHNAMURTI, R. 1970*a* On the transition to turbulent convection. Part 1. The transition from two- to three-dimensional flow, *J. Fluid Mech.* **42**, 295–307.

KRISHNAMURTI, R. 1970*b* On the transition to turbulent convection. Part 2. The transition to time-dependent flow. *J. Fluid Mech.* **42**, 309–320.

LIBCHABER, A., LAROCHE, C. & FAUVE, S. 1982 Period doubling cascade in mercury, a quantitative measurement. *J. Phys. Lett. Paris* **43**, L221–L216.

LINZ, S. J., LUKE, M., MULLER, H. W. & NIEDERLANDER, J. 1988 Convection in binary fluid mixtures: travelling waves and lateral currents. *Phys. Rev.* A **38**, 5727–5741.

LIVI, R., PETTINI, M., RUFFO, S., SPARPAGLIONE, M. & VULPIANI, A. 1985 Equipartition threshold in nonlinear large Hamiltonian systems: the Fermi–Pasta–Ulam model. *Phys. Rev.* A **31**, 1039–1045.

MALRAISON, B., ATTEN, P., BERGE, P. & DUBOIS, M. 1983 Dimension of strange attractors: an experimental determination for the chaotic regime of two chaotic systems. *J. Phys. Lett. Paris* **44**, L897–L902.

MERON, E. & PROCACCIA, I. 1986 Theory of chaos in surface waves: the reduction from hydrodynamics to few-dimensional dynamics. *Phys. Rev. Lett.* **56**, 1323–1326.

MOSES, E. & STEINBERG, V. 1986 Flow patterns and nonlinear behaviour of travelling waves in a convective binary fluid. *Phys. Rev.* A **34**, 693–696.

NICOLAENKO, B. 1987 Large scale spatial structures in two-dimensional turbulent flows. In *Proc. Intl. Conf. on the Physics of Chaos and Systems far from equilibrium, CHAOS 87* (ed. M. Duong-Van). North-Holland.

NORMAND, CH., POMEAU, Y. & VELARDE, M. G. 1977 Convective instability: a physicist's approach. *Rev. Mod. Phys.* **49**, 581–624.

OONO, Y. & KOHMOTO, M. 1985 Discrete model of chemical turbulence. *Phys. Rev. Lett.* **55**, 2927–2931.

OPPO, G. L. & KAPRAL, R. 1986 Discrete models for the formation and evolution of spatial structures in dissipative systems. *Phys. Rev.* A **33**, 4219–4231.

POCHEAU, A., CROQUETTE, V. & LE GAL, P. 1985 Turbulence in a cylindrical container of argon near threshold of convection. *Phys. Rev. Lett.* **55**, 1094–1097.

POYET, F. 1983 The Rayleigh–Bénard two-dimensional convection in a fluid between two plates of finite conductivity. PhD thesis, Columbia University.

SIMONELLI, F. & GOLLUB, J. P. 1988 In *Chaos and Complexity* (ed. A. Buiatti, S. Ciliberto, R. Livi & S. Ruffo). World Scientific.

SIMONELLI, F. & GOLLUB, J. P. 1989 Surface wave mode interactions: Effects of symmetry and degeneracy. *J. Fluid Mech.* **199**, 471–494.

STORK, K. & MÜLLER, U. 1972. Convection in boxes: experiments. *J. Fluid Mech.* **54**, 599–611.

STORK, K. & MÜLLER, U. 1975 Convection in boxes: an experimental investigation in vertical cylinders and annuli. *J. Fluid Mech.* **71**, 233–240.

TAKENS, F. 1981 Detecting strange attractors in turbulence (ed. D. A. Rand & L. S. Young). In Lecture Notes in Mathematics, vol. 808, Springer.

VASTANO, J. A. & SWINNEY, H. L. 1988 Information transport in spatiotemporal systems. *Phys. Rev. Lett.* **60**, 1773–1776.

WALDEN, R., KOLODNER, P., PASSNER, A. & SURKO, C. M. 1984 Nonchaotic Rayleigh–Bénard convection with four and five inconmensurate frequencies. *Phys. Rev. Lett.* **53**, 242–245.

WALDEN, R., KOLODNER, P., PASSNER, A. & SURKO, C. M. 1987 Heat transport by parallel roll convection in a rectangular container. *J. Fluid Mech.* **185**, 205–234.